APS physics

CHORUS

This is the accepted manuscript made available via CHORUS. The article has been published as:

Dynamic Rabi sidebands in laser-generated microplasmas: Tunability and control

R. Compton, A. Filin, D. A. Romanov, and R. J. Levis

Phys. Rev. A **83**, 053423 — Published 23 May 2011

DOI: 10.1103/PhysRevA.83.053423

Dynamic Rabi Sidebands in Laser-Generated Micro-Plasmas: Tunability and Control

R. Compton,[1,2] A. Filin,[1,2] D. A. Romanov,[1,3] and R. J. Levis[1,2]

1. Center for Advanced Photonics Research, College of Science and Technology

Temple University, Philadelphia, PA 19122

2. Department of Chemistry, Temple University, Philadelphia, PA 19122

3. Department of Physics, Temple University, Philadelphia, PA 19122

ABSTRACT

Broadband, coherent radiation in the optical frequency range is generated using micro-plasma channels in atmospheric gases in a pump-probe experiment. A micro-plasma medium is created in a gas by a focused intense femtosecond pump pulse. A picosecond probe pulse then interacts with this micro-plasma channel, producing broad, coherent sidebands that are associated with luminescence lines and are red- and blue-shifted with respect to the laser carrier frequency. These sidebands originate from the induced Rabi oscillations between pairs of excited states that are coupled by the probe pulse. Thus the sideband radiation intensity tracks the micro-plasma evolution. The sidebands arise from broad and tunable Rabi shifts corresponding to varying values of the electric field magnitude in the probe pulse. The $\sim 10^{10}$ W cm^{-2} probe beam creates a maximum sideband shift of > 90 meV from the carrier frequency, resulting in an effective bandwidth of 200 meV. The sidebands can be tuned and controlled by the intensity and temporal profile of the probe pulse. The fact that the coherence is observed in a micro-plasma demonstrates that Rabi cycling is possible at high temperature with moderately high laser intensities as long as transitions close to the driving frequency ($\Delta \sim 2\% \ \omega_c$) are available. Plasma excitation combined with Rabi-shifting measurements also serves as a means to simultaneously extract quantitative ratios for the transition dipole moments between multiple sets of highly excited states with transitions in the optical regime.

I. INTRODUCTION

The interaction of intense, tightly focused, ultrashort laser pulses with gases at atmospheric pressures results in the generation of nonequilibrium micro-plasma channels in the focal volume.[1-4] Micro-plasma evolution occurs rapidly, with electron temperature[1,2] and concentration[4-6] varying by more than an order of magnitude within the first nanosecond. These underdense plasmas (wherein the plasma frequency is smaller than the carrier frequency of a typical laser beam) are transparent and can be probed by weaker laser pulses, carrying the promise of novel linear and nonlinear optical effects. In particular, gas-component specific dynamic Rabi oscillations have been recently observed.[7] The phenomenon is marked by the generation of broad coherent sidebands and, remarkably, was observed despite plasma electron temperatures on the order of 1 eV,[1,2] where collisional dephasing might be expected to squelch any coherence.

The current understanding of the origin of the broad coherent sidebands is as follows. The cooling evolution of the micro-plasma entails considerable electronic excitation in the constituent atoms/molecules manifest by sharp luminescence lines on the background of plasma Bremsstrahlung radiation.[1] When the carrier frequency ω_c of a probe laser pulse is nearly resonant with any of these lines (with a Δ detuning), the laser field couples with the corresponding transition and induces time-dependent Rabi oscillations in the effective two-level systems. We reported the first observation of the resulting coherent broadband radiation in argon and oxygen using picosecond probe laser pulses.[7] The picosecond pulse duration provided a sufficiently short interaction time allowing Rabi cycling to compete with the electron-atom and atom-atom collisional dephasing mechanisms. Of special interest is the remarkably large bandwidth of this

coherent emission. For instance, at the probe pulse intensity of 3.3×10^{10} W cm^{-2}, a Rabi sideband shifting of > 90 meV from the carrier frequency was observed in oxygen, that results in an effectively usable bandwidth of about 200 meV.

Although perhaps the most fundamental concept in modern optics, the Rabi oscillations are rarely observed in action, because attention is typically fixed on the resulting populations of the two quantum states involved. This aspect and the implications for quantum-computing are mainly responsible for the latest revival of interest to the topic (see, e.g.[8-11]). The condition for the Rabi cycling period to be less than the characteristic decoherence time in the system was first established in nuclear magnetic resonance experiments.[12,13] Here, the energy level spacing for spin states are small (on the order of nano-eV) and coherence times are long (on the order of seconds) making control of spin-flopping facile, but also corresponding to vanishingly small frequency shifts with regard to Rabi emission. With lasers, the Rabi-related cycling was first observed in the form of "optical nutations" in the mid-IR regime, engaging ro-vibrational transitions in large molecules.[14] In the optical regime, where the frequencies involved are ~ 10^9 larger than those for NMR, a good candidate for Rabi cycling observation is alkali atom vapors, as the energy gaps between the ground and the first excited electronic state of alkali atoms are conveniently close to the frequencies of readily available driving lasers. Indeed, the first direct observation of the Rabi oscillation was made in Rb atom vapor.[15] In the spectral domain, a characteristic embodiment of Rabi oscillations was predicted[16] and observed[17,18] in the form of the so-called Mollow triplet, in which the presence of the driving laser field leads to the spontaneous fluorescence line acquiring two sidebands shifted by the Rabi frequency. The

experimentally observed shifts have been on the order of MHz (neV) to GHz (μeV).[17-19] Optical parametric amplification of Rabi sidebands at ± 3.5 meV has been attained in Na vapor using a nanosecond pump[20,21]. Later experiments extended to single atoms[22], molecules[23] and ions[24], working toward developing innovative means for information storage. Recent implementations of Rabi oscillations in solid-state systems include the manipulation of qubits in quantum dots (QDs), and excitonic state population.[11,25-28] Also, very thin GaAs films[29,30] have been used to demonstrate Rabi shifting on the order of the carrier frequency using a carrier-envelope phase stabilized femtosecond pulse. In each of these condensed-phase experiments, low temperatures had to be maintained (~10 K) to suppress excitation damping.

The Rabi sideband emission from laser-generated micro-plasmas offers two distinctive advantages as compared to the aforementioned systems. First, the method is based on transitions in the manifold of excited states and thus employs transitions with typically large values of the transition dipole moment leading to large shifts. Moreover the Rabi sidebands may occur simultaneously on multiple atomic transitions. Second, the temporal dependence and the engendered spectral interference open the way to effective control of the sidebands. In particular, the observed Rabi shifted emission driven by a ~1 ps driving pulse has a sufficient bandwidth to support much shorter ~ 14 fs temporal features.

The concept of dynamic Rabi emission and the nature of the corresponding spectra are conveniently visualized in the signature dressed-state picture shown in Figure 1. An intense laser pulse has time-dependent electric field amplitude, $A_0(t)$, and carrier frequency ω_c, shifted from the resonant frequency ω_{ab} of the two-level system by the

detuning Δ (blue shifted in the case shown). Driven by the laser field, the near-degenerate dressed states undergo time-dependent splitting by $\hbar\Omega'(t) = \hbar\sqrt{\Delta^2 + \Omega^2(t)}$ where $\Omega(t) = \mu_{ab} A_0(t)/\hbar$ is the instantaneous Rabi frequency, and μ_{ab} is the transition dipole moment. This dynamic Rabi shift results in the generation of red and blue–shifted sidebands, at instantaneous frequencies $\omega_c - \Omega'(t)$ and $\omega_c + \Omega'(t)$, respectively. The spectra of these sidebands are determined by the temporal profile of the driving pulse[31], as shown in the right panel of Figure 1. The Rabi shift reaches a maximum, $\Omega'_{\max}$, at the maximum of the driving electric field envelope ($t = t_0$). This corresponds to the points p_b and p_r of the blue- and red-shifted sidebands, respectively. Furthermore, each of the Rabi-shifted instantaneous frequency values at the front portion of the driving pulse is then repeated at the back portion of the pulse. For instance, in Figure 1 the frequencies of the sideband pulses generated at $t_0 - \delta t$ and $t_0 + \delta t$ are identical for a Gaussian temporal profile of the driving pulse ($\Omega'(t_0 - \delta t) = \Omega'(t_0 + \delta t)$). The corresponding frequency values are shown in the right panel as the points q_b and q_r in the blue- and red-shifted sidebands, respectively. The spectral amplitude at these frequencies results from the interference of the signals emitted at $t_0 - \delta t$ and $t_0 + \delta t$, thus effectuating the characteristic fringe patterns.

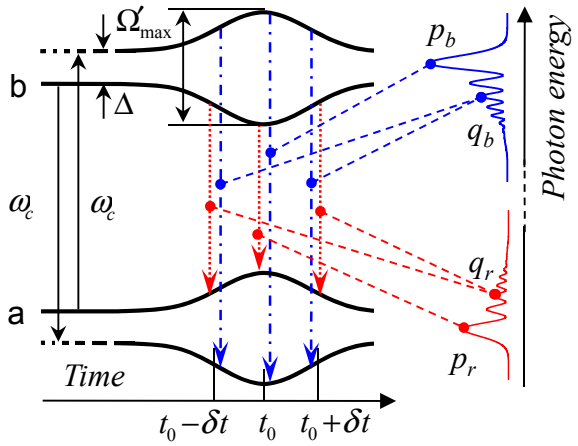

Figure 1. (Color online) A dynamic dressed-state energy level scheme for a two-level system, where levels *a* and *b* are the bare atomic states. A driving pulse with carrier frequency ω_c detuned from the resonant frequency by Δ results in a dynamic Rabi shift and in the generation of new instantaneous frequencies near the peak of the driving-pulse electric field, $\omega_c \pm \Omega'(t)$ (blue (dash-dot) and red (dot) arrows). These new frequencies form broad sidebands structured due to spectral interference as shown on the right panel.

Here, we present a systematic study of the broadband Rabi emission in the optical region, including discussion of the fundamental physical origins, the long-term dynamics tracking the plasma evolution, and, finally, possible applications hinging on the availability of spectral control. The paper is organized as follows. Section II reports the details of the experimental setup and procedures. Section III.1 presents the experimental observation of the character and trends of Rabi emission in oxygen and argon plasmas. Section III.2 presents a detailed description of the theoretical modeling that qualitatively predicts the spectrum of the sidebands as dependent on the amplitude and shape of the driving pulse. In section III.3, a model is presented to determine simultaneously the ratios of transition dipole moments between multiple excited states based on the observed dependence of the spectral positions of the sidebands on the power of the probe pulse.

The model predictions are compared with the measured functional dependencies of the sideband shifts for oxygen and argon. Section III.4 considers the characteristic fringe structure of the Rabi sidebands due to spectral interference that is controlled by the shape of the driving pulse.

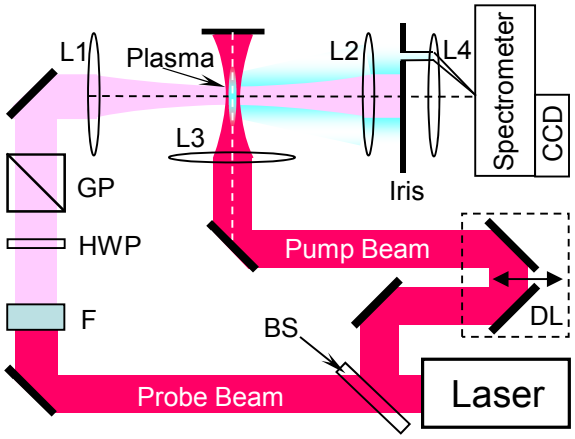

Figure 2. (Color online) Schematic of the experimental setup. L1 - L4 – lenses, GP – Glan prism analyzer, HWP – half wave plate, F – notch filter, BS – beam splitter, DL – delay line, CCD – CCD camera.

II. EXPERIMENT

A beam from a Ti:sapphire (1 kHz, 800 nm, 50 fs) laser was split 80/20 by beamsplitter BS into a horizontally polarized pump and probe beam as shown in Figure 2. The intense pump beam (~ 10^{14} Wcm^{-2}) was focused into the sample chamber (containing 1.0 atm of O_2 or Ar) using a 10 cm focal length lens L3 creating a micro-plasma medium with electron density of 10^{18}-10^{19} cm^{-3}. The pump beam was placed on an optical delay line DL in order to vary the pump/probe delay. The less intense probe beam (~ 10^{10} Wcm^{-2}) was spectrally filtered to 1 nm (centered at 800 nm) by a notch filter F and was

focused using a 25 cm focal length lens L1 overlapping with the micro-plasma. The duration of the probe beam pulse after filtering was ~1 ps. A half-wave plate HWP and Glan-prism analyzer GP were used to vary the probe beam intensity. The probe was directed at a right angle with respect to the pump beam (plasma channel) axis (interaction volume $\sim 6\times10^{-8}$ cm^3), producing red and blue-shifted Rabi sidebands that are observed close to the probe beam propagation direction. The Rabi radiation was collimated by a 25 cm focal length lens L2. Measurement of the sideband signal was made at a sufficient angle to the axis of the probe beam to suppress the contribution of the relatively intense probe beam. The angle was controlled by a translatable iris. The sideband signal that passed through the iris was directed into a spectrometer using lens L4. The spectrometer was equipped with a cooled CCD array detector.

III. RESULTS AND DISCUSSION

1. Spectra of Rabi-shifted sidebands in O_2 and Ar

Rabi cycling is typically observed in alkali metal vapors because low electronic transition energies facilitate resonant excitation using nanosecond laser sources. To detect Rabi cycling in a noble gas would require, for instance, an intense coherent source above 8 eV to drive a resonant electronic transition from the ground state. The difficulty in finding a laser source matched to the atomic Bohr frequency is remedied here by employing atomic systems that are prepared with transitions that are near resonant with an 800 nm laser source (~ 1.6 eV). With a substantial degree of excited electronic state population, low energy transitions (1-2 eV) become available for Rabi cycling using such a wavelength. We accomplish this electronic excitation using a partially ionized plasma,

resulting in numerous possible transitions in the excited state manifold. Figure 3 illustrates the continuum of electron kinetic energies formed at the onset of laser-induced plasma formation at t = 0. Electrons are initially ionized through tunnel ionization, and are subsequently driven by the laser field with energy equal to the ponderomotive energy, $U_p \sim 20$ eV. These field-driven, high kinetic energy electrons can undergo collisions with the ion core, thus establishing the initial kinetic energy distribution (or electron temperature) during the laser pulse. The electron temperature begins to evolve mainly through the mechanism of electron impact ionization cooling.[1,2] Figure 3 shows a plot of the time dependence of electron temperature in argon as calculated with the ionization cooling model presented in refs[1,2], for a plasma generated under conditions similar to those used in this experiment. The electron temperature undergoes a steep decrease in the first 300 to 400 ps after which cooling begins to taper off. Concomitant with the process of electron cooling, excited electronic states may become increasingly populated.

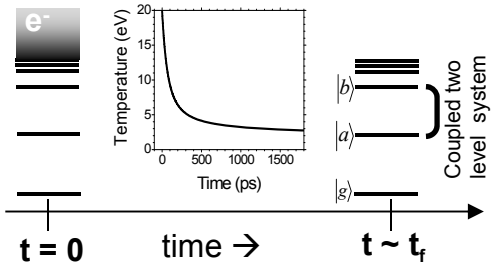

Figure 3. Schematic diagram of plasma electron cooling toward the formation of population in the excited state manifold. The pump laser beam generates a micro-plasma at t = 0 with initial electron kinetic energies ~ 20 eV. The plot in the center shows the plasma electron temperature evolution in argon following ref[1,2]. As the electron temperature decreases (by $t \sim t_f$, the value of which depends on the system parameters[2], excited electronic states become populated.

This electronic excitation formed in the plasma is manifest in the presence of multiple atomic emission lines in argon as seen in Figure 4a. These atomic lines are of constant intensity as they are dependent on the pump laser-produced plasma and exist independent of the probe beam as indicated by intensity at negative pump/probe delay. For argon, multiple transitions are observed to lie near the wavelength of the 800 nm laser used, allowing for Rabi sideband production from any of a number of possible transitions. Indeed, as the electron temperature sufficiently cools (pump/probe delay ~ 400 ps in Ar), multiple new features arise in the emission spectrum to the red and blue of each fluorescence line. These features are Rabi sidebands produced from the onset of Rabi oscillations from the states involved in the transitions. The temporal evolution of the Rabi sidebands is clearly seen in the bottom panel of Figure 4a, which shows two red-shifted sidebands centered at 803.5 nm and 815.5 nm. Thus, as the electron temperature decreases, the intensity of the sidebands also increases.

The emission spectrum of atomic oxygen as a function of pump/probe delay is shown in 4b and the experiment was performed under the same conditions as for Ar. In the spectral window only one atomic transition is observed (777 nm). In the presence of the resonance a blue-shifted Rabi sideband is seen to appear accompanied by multiple fringes (discussed later). The bottom panel of Figure 4b indicates that the temporal behavior for the main blue-shifted sideband (centered at 764 nm) and that of the remaining fringes (only the one at 760 nm is shown) is identical save for the magnitude. The rise time which can be directly correlated to the electron cooling dynamics[1,2] differs markedly from that observed in Ar. The steep rise in the oxygen Rabi sideband amplitude suggests that electron cooling occurs more rapidly than in Ar. Additionally, the oxygen

Rabi signal is observed to decay, albeit comparatively slowly relative to the rise time. This feature is not observed in Ar on the same timescale, thus suggesting dynamics specific to molecules.

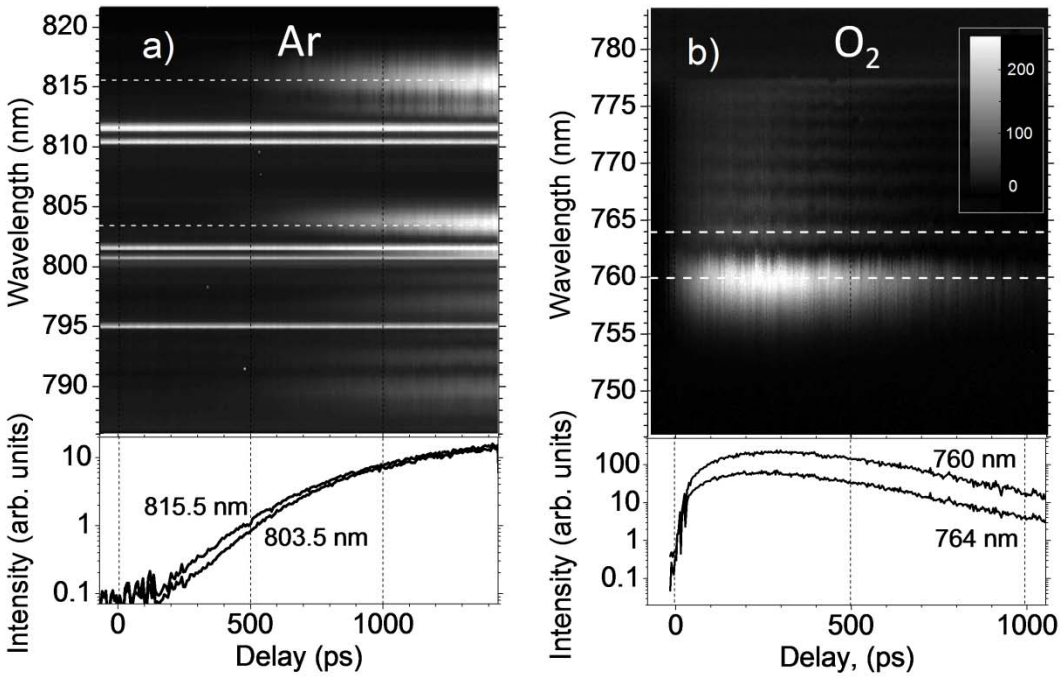

Figure 4. Comparison of the temporal evolution of the sideband emission for argon and oxygen. (a) Spectrum of argon emission as a function of pump/probe delay. Bottom panel: the intensity as a function of pump/probe delay line out of two of the red-shifted sidebands (803.5 and 815.5 nm). (b) Spectrum of atomic oxygen emission as a function of pump/probe delay. Bottom panel: the intensity as a function of pump/probe delay line out for two fringes (760 and 764 nm) originating from a single blue-shifted Rabi sidebands. White dashed lines correspond to the spectral positions for the presented decay curves.

2. Time-dependent, generalized Rabi cycling model

The generation of dynamic Rabi sidebands as observed in Figure 4a and b can be quantitatively described in the context of a time-dependent, generalized Rabi-cycling

model. It relates to the model of optical nutation suggested previously.[32,33] The FWHM duration of the driving pulse is about 1 ps, which is shorter than both the diagonal relaxation time (i.e., the excited states lifetime) and the dephasing time that is mainly determined by the electron-atom collisions in the cooling plasma. This circumstance makes it sufficient to consider the wavefunction evolution

$$\left|\Psi\right\rangle = c_a\left(t\right)\exp\left(-i\,E_a t/\hbar\right)\left|a\right\rangle + c_b\left(t\right)\exp\left(-i\,E_b t/\hbar\right)\left|b\right\rangle \tag{1}$$

rather than tracing the Bloch vector. The time-dependent amplitude and frequency of the generated radiation will be determined by the induced dipole oscillations, that is, by the instantaneous expectation value of the dipole moment operator,

$$\left\langle\hat{\mu}\right\rangle = \left\langle\psi\left|\hat{\mu}\right|\psi\right\rangle = c_a^*(t)c_b(t)\mu_{ab}e^{-i\omega_{ba}t} + \text{c.c.}, \tag{2}$$

where $\omega_{ba} = \left(E_b - E_a\right)/\hbar$ is the transition frequency and $\mu_{ab} = \left\langle a\left|\hat{\mu}\right|b\right\rangle$ is the transition dipole moment.

In the rotating wave approximation, the coefficients in the rotating frame, $\tilde{c}_a\left(t\right) = c_a\left(t\right)\exp\left(-it\,\omega_c/2\right)$ and $\tilde{c}_b\left(t\right) = c_b\left(t\right)\exp\left(it\,\omega_c/2\right)$ are determined by the coupled equations,

$$i\frac{d}{dt}\begin{pmatrix}\tilde{c}_a\\ \\ \tilde{c}_b\end{pmatrix} = \begin{pmatrix}-\dfrac{\Delta}{2} & -\dfrac{\Omega(t)}{2}\\ -\dfrac{\Omega(t)}{2} & \dfrac{\Delta}{2}\end{pmatrix}\begin{pmatrix}\tilde{c}_a\\ \\ \tilde{c}_b\end{pmatrix} = \frac{1}{2}\frac{\Delta}{\cos\alpha}\begin{pmatrix}-\cos\alpha & -\sin\alpha\\ -\sin\alpha & \cos\alpha\end{pmatrix}\begin{pmatrix}\tilde{c}_a\\ \tilde{c}_b\end{pmatrix}. \tag{3}$$

Here, $\Delta = \omega_{ba} - \omega_c$ is the detuning from the resonance, while $\Omega(t) = \mu_{ab}A_0(t)/\hbar$ is the time-dependent Rabi frequency, determined by the electric field envelope, $A_0\left(t\right)$. The time-dependent parameter α is defined as $\alpha(t) = \tan^{-1}\left(\Omega\left(t\right)/\Delta\right)$, provided nonzero detuning Δ. Then, it is convenient to recast Eq. (3) in the adiabatic basis:[34,35]

$$\begin{pmatrix} \bar{c}_a \\ \\ \bar{c}_b \end{pmatrix} = \begin{pmatrix} \cos\left(\frac{\alpha}{2}\right) & \sin\left(\frac{\alpha}{2}\right) \\ -\sin\left(\frac{\alpha}{2}\right) & \cos\left(\frac{\alpha}{2}\right) \end{pmatrix} \begin{pmatrix} \tilde{c}_a \\ \\ \tilde{c}_b \end{pmatrix} \tag{4}$$

The coefficients $\bar{c}_a$, $\bar{c}_b$ satisfy the more simple system of equations,

$$i\frac{d}{dt}\begin{pmatrix} \bar{c}_a \\ \bar{c}_b \end{pmatrix} = \frac{1}{2}\frac{\Delta}{\cos\alpha}\begin{pmatrix} -1 & 0 \\ 0 & 1 \end{pmatrix}\begin{pmatrix} \bar{c}_a \\ \bar{c}_b \end{pmatrix} - \frac{i}{4}\frac{d\alpha}{dt}\begin{pmatrix} 0 & -1 \\ 1 & 0 \end{pmatrix}\begin{pmatrix} \bar{c}_a \\ \bar{c}_b \end{pmatrix}, \tag{5}$$

where the second term in the right-hand side is responsible for nonadiabatic corrections.

If

$$\left|\frac{d\alpha}{dt}\right| << \frac{2\Delta}{\cos\alpha}, \tag{6}$$

this term can be neglected, and the solution is readily obtained as,

$$\begin{pmatrix} \tilde{c}_a(t) \\ \\ \tilde{c}_b(t) \end{pmatrix} = \begin{pmatrix} \cos\left(\frac{\alpha}{2}\right) & -\sin\left(\frac{\alpha}{2}\right) \\ \sin\left(\frac{\alpha}{2}\right) & \cos\left(\frac{\alpha}{2}\right) \end{pmatrix} \begin{pmatrix} e^{i\varphi(t)} & 0 \\ 0 & e^{-i\varphi(t)} \end{pmatrix} \begin{pmatrix} \cos\left(\frac{\alpha_0}{2}\right) & \sin\left(\frac{\alpha_0}{2}\right) \\ -\sin\left(\frac{\alpha_0}{2}\right) & \cos\left(\frac{\alpha_0}{2}\right) \end{pmatrix} \begin{pmatrix} \tilde{c}_a(t_0) \\ \\ \tilde{c}_b(t_0) \end{pmatrix}, \tag{7}$$

where

$$\varphi(t) = \int_{t_0}^{t} dt' \frac{\Delta}{2\cos\alpha} = \frac{1}{2}\int_{t_0}^{t} dt' \sqrt{\Delta^2 + \Omega^2(t)} \tag{8}$$

and $\alpha_0 = \alpha(t_0)$. In particular, if the two-level system was initially in its lower state, $c_a(t_0) = 1$, $c_b(t_0) = 0$, this results in the following expression for the time-dependent coefficients:

$$\begin{pmatrix} \tilde{c}_a(t) \\ \\ \tilde{c}_b(t) \end{pmatrix} = \begin{pmatrix} \cos\left(\frac{\alpha}{2}\right)\cos\left(\frac{\alpha_0}{2}\right)e^{i\varphi(t)} + \sin\left(\frac{\alpha}{2}\right)\sin\left(\frac{\alpha_0}{2}\right)e^{-i\varphi(t)} \\ \sin\left(\frac{\alpha}{2}\right)\cos\left(\frac{\alpha_0}{2}\right)e^{i\varphi(t)} - \cos\left(\frac{\alpha}{2}\right)\sin\left(\frac{\alpha_0}{2}\right)e^{-i\varphi(t)} \end{pmatrix} \tag{9}$$

Then, the dipole oscillations are obtained as

$$\mu(t) = \mu_{ab}\Big(\sin(\alpha)\cos(\alpha_0)\cos(\omega_c t) - \frac{1}{2}\sin(\alpha_0)\big(1+\cos(\alpha)\big)\cos\big(2\varphi(t)+\omega_c t\big) - \frac{1}{2}\sin(\alpha_0)\big(1-\cos(\alpha)\big)\cos\big(2\varphi(t)-\omega_c t\big)\Big) \tag{10}$$

Returning to conventional notation, we obtain the oscillating dipole as

$$\mu(t) = \frac{\mu_{ab}}{\Omega'(t_0)}\Bigg[\frac{\Delta\Omega(t)}{\Omega'(t)}\cos(\omega_c t) - \frac{\Omega(t_0)}{2}\left(\frac{\Delta}{\Omega'(t)}+1\right)\cos\left(\omega_c t + \int_{t_0}^{t} dt'\sqrt{\Delta^2+\Omega^2(t)}\right) - \frac{\Omega(t_0)}{2}\left(\frac{\Delta}{\Omega'(t)}-1\right)\cos\left(\omega_c t - \int_{t_0}^{t} dt'\sqrt{\Delta^2+\Omega^2(t)}\right)\Bigg] \tag{11}$$

The arguments of the cosines in the second and the third lines of Eq. (11) signify the presence of emitted radiation with instantaneous frequencies,

$$\omega_{\pm}(t) = \omega_c \pm 2\,d\varphi/dt = \omega_c \pm \sqrt{\Delta^2+\Omega^2(t)} = \omega_c \pm \Omega'(t), \tag{12}$$

that form the blue-shifted and red-shifted Rabi sidebands as exhibited in Figure 4. We note in passing that if the adiabaticity condition of Eq. (6) were maintained over the whole duration of the driving pulse, it would mean $\alpha_0 = \alpha(t_0) = 0$ in Eq. (7) and $\Omega(t_0) = 0$ in Eq. (11). Then, the two-level system being initially in the ground state would undergo adiabatic following and no sideband emission would occur. However, the actual position of the adiabaticity onset point, t_0, affects only the overall magnitude of the sideband emission. The emission frequencies and spectral phase relations discussed later are insensitive to the value of t_0. For certainty, in what follows, we assume t_0 to be

the point of maximum derivative of the function $A_0(t)$, which corresponds to the inflection point in Figure 1.

This model predicts that two new sidebands will be generated with instantaneous frequencies $\omega_c \pm \Omega'(t)$, as related to the second and the third line in Eq. (11). Over the probe pulse duration, the sideband frequencies will cover significant intervals of width $\sqrt{\Delta^2 + \Omega_{\max}^2} - \Delta$, where $\Omega_{\max}$ is the maximum Rabi frequency that corresponds to the maximum electric field magnitude in the probe pulse, $A_{0\max}$. As the value of $A_{0\max}$ increases, one sideband will begin shifting along the frequency axis away from the fluorescence line that is detuned by Δ from the probe pulse carrier frequency. The other sideband will emerge on the other side of the carrier frequency at a position mirroring the fluorescence peak and begin shifting in the opposite direction, thus increasing the inter-sideband separation. The two sidebands will be centered about the carrier frequency of the probe beam. One sideband is predicted to have larger amplitude than the other according to the ratio of their prefactors in Eq. (11), $\Delta/\Omega'(t)+1$ and $\Delta/\Omega'(t)-1$. In particular, the intensity of the mirrored sideband (corresponding to of the $\Delta/\Omega'(t)-1$ prefactor) rapidly converges to zero in the limit of low intensity of the generating probe beam.

3. Rabi sidebands vs. laser power: tunable broadband radiation and transition dipole extraction

The predictions of the model have been quantitatively verified in a pump-probe experiment involving oxygen. In the case of atomic oxygen there is only one resolved

luminescence line in the vicinity of the laser carrier frequency. In this situation, the presence of the mirrored sideband will not be obfuscated by effects of other transitions as is the case in argon for instance. When the micro-plasma is generated in molecular oxygen and undergoes cooling evolution, atomic oxygen is created with population in the excited state manifold. Of particular interest are the ^5P and $^5S^0$ states, which have intense dipole coupling, resulting in three closely spaced (< 1 meV difference) fluorescence lines near 777 nm (1.596 eV). This unresolved triplet is detuned from the 800 nm probe beam by 46 meV. As a result of the interaction of a probe beam with the oxygen plasma, the blue- and red-shifted sidebands emerge in the spectrum, as reported in ref[7]. With a 1.05 mW probe, the intense blue-side broadband emission is centered on 1.643 eV. This is consistent with the prediction of our model, assuming an effective transition dipole of 7.4 D, a detuning of 46 meV, and the focal intensity of 3.3×10^{10} W cm^{-2}. The red-shifted sideband mirrors the shift and the shape of the blue-shifted feature. However, the amplitude of the red-shifted sideband is markedly smaller. This is in complete agreement with the predictions of Eq. (11), where the outer boundaries of both the red and blue sidebands are shifted (in opposite directions) by the maximum generalized Rabi frequency, $\Omega'_{\max}$, while their amplitudes differ considerably from one another as predicted by the pre-factors for the oscillating terms. Further, the intensity of the Rabi sidebands in oxygen plasma peaks at the pump/probe delay of 250 ps (Figure 4b, bottom panel). This considerable delay ensures that the electronic excitation of oxygen atoms is maximized in the generated plasma and that the electron temperature is concurrently reduced,[1] so that the dephasing dominated by the electron-neutral collisions becomes negligible ($\tau \geq 20$ ps).

In further quantitative agreement with the theoretical model, the measurements shown in Figure 5 (a) demonstrate that the blue sideband shifts further from the carrier frequency as the probe beam power is increased from 0.1 to 1.0 mW. This increase in power corresponds to an increase in the focal intensity from 3.3×10^{9} W cm^{-2} to 3.3×10^{10} W cm^{-2}, effecting the corresponding increase in the maximum generalized Rabi frequency, $\Omega'_{\max}$. The observed shift constitutes an apparent means for providing tunable coherent radiation from 1.596 eV to 1.640 eV for this particular transition. (The fringes seen in the low-energy wing of the blue-shifted sideband in Figure 5 (a) (and mirrored in the high-energy wing of the red-shifted sideband) are the result of spectral interference that will be discussed in detail in Section III.4.)

As shown in Figure 4a, sidebands are efficiently generated from all fluorescence transitions near the 800 nm probe according to Eq. (11), provided the detuning is not too large to drive the amplitude of the generalized Rabi frequency to zero. Sidebands appear simultaneously in Ar for the three spectral regions labeled A, B and C in Fig. 5 (b). Sideband C is generated from the fluorescence line on the high-energy side of the probe and exhibits similar behavior to the oxygen system with a blue-shifted signal originating from the fluorescence line. However, for transitions A and B which are on the low-energy side of the probe photon energy, red-shifted lines are seen to emerge from the fluorescence transition. This observation is consistent with Eq. (11) where the amplitudes of the red and blue-shifted sidebands reflect the sign of the detuning, Δ.

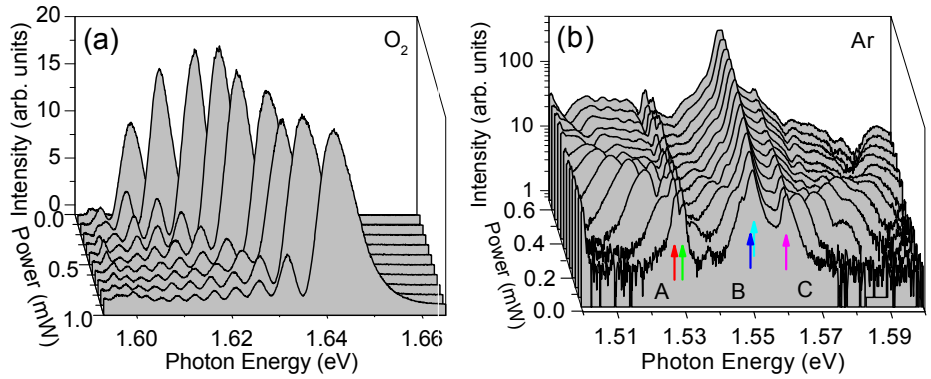

Figure 5. (Color online) Comparison of the functional dependencies of the sidebands on the driving laser power for oxygen and argon. (a) Spectra of the blue-shifted sideband for selected probe beam intensities in oxygen. The spectra are taken at a pump/probe delay of 250 ps. (b). Ar spectra for selected probe beam intensities. The spectra are taken at a pump/probe delay of 1400 ps. The arrows correspond to atomic fluorescence lines at 1.5271 eV (red), 1.5280 eV (green), 1.5302 eV (dark blue), 1.5488 eV (light blue), and 1.5601 eV (magenta).

According to Eq. (11), the dependence of the maximum shift energy of the sideband on the probe laser power can be expressed as,

$$E_{peak} = \frac{\Delta}{|\Delta|}\left(kP + (\hbar\Delta)^2\right)^{1/2} + \hbar\omega_c , \tag{13}$$

where P is the peak probe laser power, $(kP)^{1/2} = \hbar\Omega$, and $k^{1/2}$ is the slope of the linear dependence of $\hbar\Omega$ on $P^{1/2}$. The ratio of the transition dipole moment for any two transitions can then be determined using the ratio of the $k^{1/2}$ values.

Figure 6 (a) shows a plot of the sideband energy as a function of probe power. Again, the sidebands arising in regions A and B exhibit a red-shift, indicated by the fit using Eq. (13) where at negative Δ the value of E_{peak} decreases with increasing probe power. The value of E_{peak} for the blue-shifted sideband C increases with probe power. The mirror features of sidebands A, B and C are difficult to see as their intensities are

about an order of magnitude smaller than the main features. In addition, they are largely obscured by interference from sidebands arising from adjacent transitions.

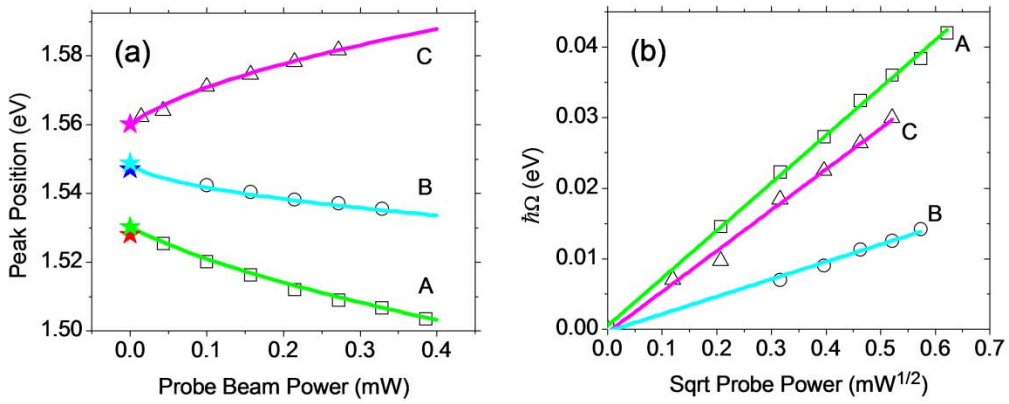

Figure 6.(Color online) (a) Plot of the sideband energy, E_{peak} , as a function of probe beam power corresponding to the measurements in Figure 5 (b). The stars indicate the fluorescence line positions, labeled A, B and C from Figure 5 (b), from which Rabi sidebands originate. The solid curves are the fit using Eq. (13). (b) Plot of $\hbar\Omega$ as a function of the square root of the probe beam power (extracted from (a)). The solid curve is the best linear fit. The slope yields the value $k^{1/2}$ from Eq. (13).

Literature values[36] for the ratio of the transition dipole moments for transition C with the two transitions for A yield values of 1.06 and 1.45. Similarly, the ratio of transition C with the lines constituting B gives 2.42 and 2.59. Comparison with the ratios of the $k^{1/2}$ values, extracted from a plot of $\hbar\Omega$ vs. the square root of the probe power is shown in Figure 6 (b) for the same lines gives $k_C^{1/2}/k_A^{1/2} = 0.86$ and $k_C^{1/2}/k_B^{1/2} = 2.23$. By using the ratios of the $k^{1/2}$ values, this method avoids the inherent difficulties often encountered in performing accurate measurements of the laser intensity. The agreement with the literature values (known to within $\pm$ 10%)[36] demonstrates that plasma excitation combined with Rabi-shifting measurements can serve as a means to simultaneously

extract quantitative ratios for the transition dipole moments between multiple sets of highly excited states with transitions in the optical regime.

4. Spectral interference and pulse-compression prospects

The shifting of the sidebands gives rise to bandwidths on the order of 200 meV. Each particular frequency value within those bands is emitted at a certain amplitude value of the driving pulse. If coherence can be maintained across this spectral range, the light can be shaped and manipulated for applications such as control experiments and short pulse generation. In fact, there is an indication that the sidebands generated in these experiments possess a high degree of coherence across the whole spectral range. This coherence is manifest in the characteristic fringe pattern exhibited in the sidebands as clearly seen in Figures 4 (b) and 5 (a). Indeed, these fringes result from spectral interference of like frequency components emitted at different moments of time. According to Eq. (11), the points of the same electric field amplitude on the leading and trailing edges of the probe pulse generate waves of the same instantaneous frequency that then may interfere constructively or destructively. The spectral positions for destructive interference can be approximately predicted as follows. The maximum of the temporal envelope profile of the probe pulse generates the maximum value of the instantaneous generalized Rabi frequency, $\Omega'_{\max}$ that lies within the main peak of the respective sideband (that is, the peak at the maximally shifted position, Figure 7, upper panel). The lower-magnitude regions of the temporal profile of the probe pulse generate the frequencies, $\Omega'(t)$, that correspond to time-dependent Rabi shifts and produce the features between the main peak and the oxygen fluorescence line at 1.596 eV. Near the

maximum amplitude of the laser pulse, the temporal envelope profile may be approximated by a parabola, $A_0(t) \approx A_{\max} - \beta(t-\tau_0)^2$ (Figure 7, lower panel). (for instance, for the Gaussian pulse shape in Figure 1, $A_0(t) = A_{\max}\exp\left(-(t-\tau_0)^2/\sigma^2\right)$, the value of β is $A_{\max}/\sigma^2$). Then, the waves of a given sideband shift value, Ω', are generated on the leading and the trailing edges of the probe pulse at the moments $t_{1,2} = t_0 \mp (\Omega_{\max} - \Omega)^{1/2}/(\mu_{ab}\beta)^{1/2}$. For destructive interference, the phase difference between these waves due to the driven dipole moment evolution from t_1 to t_2 should be equal to $\pi(2n+1)$. This condition determines the values of Ω' at which the destructive interference occurs,

$$\Omega'_{\max} - \Omega' = \left(\frac{3\pi}{4}\right)^{2/3}\left(\frac{\mu_{ab}\beta}{\hbar}\frac{\Omega_{\max}}{\Omega'_{\max}}\right)^{1/3}(2n+1)^{2/3}. \qquad (14)$$

Within this approximation, the distinction between two consecutive fringe minima in Figure 7 can be crudely predicted using the relation, $\Delta E_n = b\left((2n+1)^{2/3} - (2n-1)^{2/3}\right)$ where E_n denotes the energy of the n-th fringe minimum and b is a fitting parameter (in the aforementioned case of the Gaussian pulse shape, this fitting parameter is related to the pulse and molecule characteristics as $b = \hbar(3\pi/4)^{2/3}\left(\left((\Omega'_{\max})^2 - \Delta^2\right)/\left(\Omega'_{\max}\sigma^2\right)\right)^{1/3}$). The excellent correlation between this simple model prediction and the experimental results is seen in the top panel of Figure 7 where the positions of destructive interference are indicated by black semi-circles. Each semi-circle corresponds to a pair of symmetric points (indicated by open squares) in the (parabolic) temporal profile of the probe pulse envelope from which two identical values

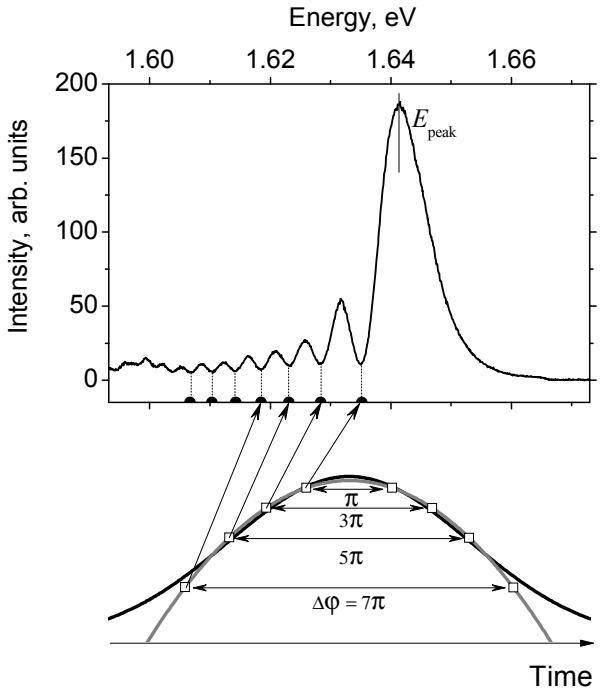

Figure 7. The origin of the spectral fringes. The upper panel: a typical spectrum of the blue-shifted Rabi sideband (oxygen, probe beam power P = 1.0 mW). The black semi-circles indicate regions of destructive interference as predicted using Eq. (14). The lower panel: an ideal Gaussian temporal profile of the probe beam (black curve) and the parabolic approximation used to derive Eq. (14) (gray curve). The squares show schematically the pairs of points with equal probe beam intensity and a phase difference of $\Delta\varphi = (2n+1)\pi$, where $n = 0, 1, 2, \ldots$, in the induced dipole oscillations. Each of these pairs corresponds to a point of destructive interference in the upper panel. The maximum generalized Rabi shift $E_{peak} = \hbar\Omega'_{max}$, as reconstructed using Eq. (14), is also indicated.

of Rabi shift are generated. When the phase difference between the two points in such a Rabi shifted pair is equal to an odd integer multiple of π, full destructive interference is observed. Moreover, once the value of the fitting parameter b is established, Eq. (14) allows us to find the exact position of the maximum generalized Rabi shift, $E_{peak} = \hbar\Omega'_{max}$, within the main sideband peak. As seen in Figure 7, this position corresponds to the main peak maximum with high accuracy; the result corroborates the dependence of the peak maximum shift with the probe laser power as discussed earlier in relation to Figures 5

and 6. This simplified approach has been verified by a model that allows for simulation of the Rabi sideband spectra and provides the means for spectral phase reconstruction.[31] From this standpoint, the fringe patterns persisting throughout both the blue-shifted and red-shifted sidebands indicate that all of the radiation generated through the Rabi-cycling mechanism is essentially coherent. Thus, the giant Rabi shifting represents a novel source of broadband, tunable, ultrafast radiation generated conveniently by means of a femtosecond laser-induced micro-plasma and a moderately-intense picosecond probe beam.

IV. CONCLUSIONS

Micro-plasma channels formed in gases at atmospheric pressure in the wake of focused laser pulses provide a novel mechanism for generating broadband coherent radiation in the optical frequency range. The mechanism is based on giant, time-dependent Rabi shifting produced by a moderately intense picosecond laser pulse. The viability and robustness of the proposed approach are demonstrated in a series of pump-probe experiments in an oxygen micro-plasma. The red- and blue-shifted sidebands (with respect to the laser carrier frequency) are observed with the maximum shift of > 90 meV, resulting in an effective bandwidth of 200 meV. The giant Rabi shift is both tunable and coherent over a wide range of frequencies and over a wide range of atomic transitions. The tunability is based on the time-dependent generalized Rabi frequency and thus depends only on the intensity of the driving laser. The fact that the coherence is observed in a micro-plasma demonstrates that Rabi cycling is possible at high temperature with moderately high laser intensities (10^{10} W cm^{-2}) as long as transitions close to the driving frequency ($\Delta \sim 2\% \, \omega_c$) are present.

AKNOWLEGMENTS

We acknowledge the support of the Army Research Office through Award # W911NF0810020 and the National Science Foundation CHE0518497. The authors would also like to thank Dr. M. Plewicki and Dr. I.S. Averbukh for helpful discussions.

REFERENCES

1 Filin, A., Compton, R., Romanov, D. A. & Levis, R. J. Impact-Ionization Cooling in Laser-Induced Plasma Filaments. *Physical Review Letters* **102**, 155004, 155004 (2009).

2 Romanov, D. A., Compton, R., Filin, A. & Levis, R. J. Dynamics of strong-field laser-induced microplasma formation in noble gases. *Physical Review A* **81**, 033403 (2010).

3 Theberge, F., Liu, W. W., Simard, P. T., Becker, A. & Chin, S. L. Plasma density inside a femtosecond laser filament in air: Strong dependence on external focusing. *Physical Review E* **74**, 036406, 036406 (2006).

4 Liu, J. S. *et al.* Time-resolved investigation of low-density plasma channels produced by a kilohertz femtosecond laser in air. *Physical Review E* **72**, 026412, 026412 (2005).

5 Tzortzakis, S., Prade, B., Franco, M. & Mysyrowicz, A. Time-evolution of the plasma channel at the trail of a self-guided IR femtosecond laser pulse in air. *Optics Communications* **181**, 123-127 (2000).

6 Rodriguez, G., Valenzuela, A. R., Yellampalle, B., Schmitt, M. J. & Kim, K. Y. In-line holographic imaging and electron density extraction of ultrafast ionized air filaments. *Journal of the Optical Society of America B-Optical Physics* **25**, 1988-1997 (2008).

7 Compton, R., Filin, A., Romanov, D. A. & Levis, R. J. Observation of Broadband Time-Dependent Rabi Shifting in Microplasmas. *Physical Review Letters* **103**, 205001 (2009).

8 Miroshnychenko, Y. *et al.* Coherent excitation of a single atom to a Rydberg state. *Physical Review A* **82**, 013405 (2010).

9 Chiorescu, I., Nakamura, Y., Harmans, C. & Mooij, J. E. Coherent quantum dynamics of a superconducting flux qubit. *Science* **299**, 1869-1871 (2003).

10 Yu, Y., Han, S. Y., Chu, X., Chu, S. I. & Wang, Z. Coherent temporal oscillations of macroscopic quantum states in a Josephson junction. *Science* **296**, 889-892 (2002).

11 Stievater, T. H. *et al.* Rabi oscillations of excitons in single quantum dots. *Physical Review Letters* **87**, 133603 (2001).

12 Rabi, I. I. Space quantization in a gyrating magnetic field. *Physical Review* **51**, 652-654 (1937).

13 Rabi, I. I., Millman, S., Kusch, P. & Zacharias, J. R. The molecular beam resonance method for measuring nuclear magnetic - Moments the magnetic moments of Li-3(6) Li-3(7) and F-9(19). *Physical Review* **55**, 526-535 (1939).

14 Hocker, G. B. & Tang, C. L. Observation of optical transient nutation effect. *Physical Review Letters* **21**, 591 (1968).

15 Gibbs, H. M. Spontaneous Decay of Coherently Excited Rb. *Physical Review Letters* **29**, 459-& (1972).

16 Mollow, B. R. Power Spectrum of Light Scattering by Two-Level Systems. *Physical Review* **188**, 1969 (1969).

17 Schuda, F., Stroud, C. R. & Hercher, M. Observation of Resonant Stark Effect at Optical Frequencies. *Journal of Physics B-Atomic Molecular and Optical Physics* **7**, L198-L202 (1974).

18 Wu, F. Y., Grove, R. E. & Ezekiel, S. Investigation of Spectrum of Resonance Fluorescence Induced by a Monochromatic Field. *Physical Review Letters* **35**, 1426-1429 (1975).

19 Flagg, E. B. *et al.* Resonantly driven coherent oscillations in a solid-state quantum emitter. *Nature Physics* **5**, 203-207 (2009).

20 Harter, D. J., Narum, P., Raymer, M. G. & Boyd, R. W. Four-Wave Parametric Amplification of Rabi Sidebands in Sodium. *Physical Review Letters* **46**, 1192-1195 (1981).

21 Harter, D. J. & Boyd, R. W. Four-wave mixing resonantly enhanced by ac-Stark-split levels in self-trapped filaments of light. *Physical Review A* **29**, 739 (1984).

22 Darquie, B. *et al.* Controlled single-photon emission from a single trapped two-level atom. *Science* **309**, 454-456 (2005).

23 Gerhardt, I. *et al.* Coherent state preparation and observation of Rabi oscillations in a single molecule. *Physical Review A* **79**, 011402 (2009).

24 Roos, C. *et al.* Quantum state engineering on an optical transition and decoherence in a Paul trap. *Physical Review Letters* **83**, 4713-4716 (1999).

25 Kamada, H., Gotoh, H., Temmyo, J., Takagahara, T. & Ando, H. Exciton Rabi oscillation in a single quantum dot. *Physical Review Letters* **87**, 246401 (2001).

26 Zrenner, A. *et al.* Coherent properties of a two-level system based on a quantum-dot photodiode. *Nature* **418**, 612-614 (2002).

27 Xu, X. D. *et al.* Coherent optical spectroscopy of a strongly driven quantum dot. *Science* **317**, 929-932 (2007).

28 Melet, R. *et al.* Resonant excitonic emission of a single quantum dot in the Rabi regime. *Physical Review B* **78**, 073301 (2008).

29 Vu, Q. T. *et al.* Light-induced gaps in semiconductor band-to-band transitions. *Physical Review Letters* **92**, 217403 (2004).

30 Mucke, O. D. *et al.* Carrier-wave Rabi flopping: role of the carrier-envelope phase. *Optics Letters* **29**, 2160-2162 (2004).

31 Plewicki, M., Compton, R., Filin, A., Romanov, D. A. & Levis, R. J. Origin of the spectral coherence in dynamically broadened Rabi sidebands. *Optics Letters* **35**, 778-780 (2010).
32 Boyd, R. W. *Nonlinear Optics*. 3 edn, (Academic Press, 2008).
33 Akulin, V. M. & Karlov, N. V. *Intense Resonant Interactions in Quantum Electronics*. (Springer-Verlag, 1992).
34 Tannor, D. J. *Introduction to Quantum Mechanics: A Time-Dependent Perspective*. (University Science Books, 2007).
35 Averbukh, I. S. & Perelman, N. F. Quasi-energy and optical-spectra of a 2-level system in a low-frequency field of arbitrary strength. *Zhurnal Eksperimentalnoi I Teoreticheskoi Fiziki* **88**, 1131-1146 (1985).
36 Shumaker, J. B. & Popenoe, C. H. Experimental Transition Probabilities for Ar I 4s-4p Array. *Journal of the Optical Society of America* **57**, 8 (1967).